INTERNATIONAL JOURNAL FOR NUMERICAL METHODS IN FLUIDS
Int. J. Numer. Meth. Fluids 2004; **44**:209–230 (DOI: 10.1002/fld.637)

Finite element analysis of filling stage in die-casting process using marker surface method and adaptive grid refinement technique

J. H. Jeong[1,*,†] and D. Y. Yang[2]

[1]*Department of Intelligent Precision Machine, Korea Institute of Machinery and Materials, Daejeon, Korea*
[2]*Department of Mechanical Engineering, Korea Advanced Institute of Science and Technology, Daejeon, Korea*

SUMMARY

The marker surface method and the adaptive grid refinement technique have been applied to the three-dimensional (3-D) finite element analysis of the filling stage in the die-casting process. Especially, the marker surface plugging technique and the marker surface regeneration technique incorporated in the marker surface method have been proposed for the efficient analysis of 3-D practical problems. Through the marker surface plugging technique, new parts of marker surface are effectively created in order to eliminate the gaps between the parts of marker surface or between the edge of marker surface and cavity wall. By using the marker surface regeneration technique, the marker surface including a great number of marker elements is recreated on the basis of its original shape in order to decrease the number of marker elements and computational time. A 3-D example used as the benchmark test and a typical industrial problem of the die-casting process have been analysed. The numerical results have been in good agreement with the experimental results and the efficiency of the adaptive grid refinement technique has been verified. It has been shown that the proposed techniques incorporated in the marker surface method and the adaptive grid refinement technique can be effectively applied to general industrial problems. Copyright © 2004 John Wiley & Sons, Ltd.

KEY WORDS: finite element; marker surface method; adaptive grid refinement; die-casting

1. INTRODUCTION

In the die-casting process, molten metal is injected into the die cavity at high speed and is held under high pressure during the solidification stage. Therefore, as compared to the permanent mold casting, the geometric dimension of the products of the die-casting process is more precise and the cycle time is much shorter. The finite difference method (FDM) has been employed in simulating molten metal flow for general practical problems of the casting

---

[*] Correspondence to: J. H. Jeong, Nanomechanisms Group, Department of Intelligent Precision Machine, Korea Institute of Machinery and Materials, P.O. Box 101, Yusong, Daejeon, Korea.

[†] E-mail: jhjeong@kimm.re.kr

Received 14 August 2002
Revised 18 August 2003

processes. Recently, the finite element method (FEM) is being applied to the mold filling analysis. The FEM has several advantages over the FDM in the analysis of the die-casting process in which the die cavity with complex shape and thin wall is required. First, the geometry of two-dimensional (2-D) and 3-D curved surfaces can be accurately described and the skew boundary condition can be imposed on the surface. Secondly, the initial grid can be efficiently created by the element density control.

In order to represent the transient melt flow with free surface in the filling stage, typically, the marker particle method and the volume of fluid (VOF) method have been used. In the marker particle method, there are the marker and cell (MAC) method in which the marker concept was introduced by Harlow and Welch [1] in 1965 and the simplified marker and cell (SMAC) method, as a modified version of the MAC, presented by Amsden and Harlow [2] in 1970. In 1988, Hwang and Stoehr [3] used the SMAC method based on the FDM to simulate 2-D mold filling phenomena and their work included the effects of turbulence and wall shear stress. In 1988, Anzai and Niyama [4] analysed the filling stage of the die-casting process by using the Hicass/flow system in which the SMAC method and quasi 3-D filling model were employed. In 1990, for analysing the aluminium die-casting process, Anzai and Uchida [5] presented the modified quasi 3-D model. In 1990, Hwang *et al.* [6] proposed a new mathematical model based on the solution algorithm-marker and cell (SOLA-MAC) method. Through the model the flow phenomenon of a rotating mold with water was analysed. In 1991 Nomura and Terashima [7] used the SMAC method to analyse the filling stage in the die-casting process. They then discussed the filling characteristics in the practical die-casting process by comparing the predicted free surface and experimental surface line. In 1993 Chen *et al.* [8] demonstrated that the solution algorithm-volume of fluid (SOLA-VOF) method is more reasonable and efficient than the SOLA-MAC method to analyse the mold filling phenomenon with high speed. In 1997, Zaidi *et al.* [9] simulated the mold filling using the FEM, the marker particle method and the k–ε turbulent model.

In the marker particle method, in order to reduce the memory storage and computation time required for the analysis of 2-D and 3-D problems, Hwang and Stoehr [10] proposed the marker reduction technique where the number of marker particles is decreased through deletion of marker particles in the internal fluid region, and Chen *et al.* [11] presented the surface marker (SM) method for 2-D problems, in which a single string of marker particles along the free surface is used. In order to represent 2-D free surface more accurately, Nichols and Hirt [12] and Wang and Stuhmiiler [13] used linear surface segments to connect marker particles. In 1998 Jeong and Yang [14] proposed the marker surface method in which the fluid flow is represented by a marker surface composed of marker elements instead of marker particles, to carry out 3-D finite element analyses of fluid flow with free surface more effectively.

The adaptive grid refinement techniques based on the FEM have been used in several fields of fluid flow analysis and the efficiency of the techniques has been proven. In 1986 Oden *et al.* [15] presented the adaptive finite element method for analysing unsteady inviscid compressible flow in arbitrary 2-D domains. The method includes the h-method, in which the grid is refined or unrefined, and the r-method in which the mesh is automatically distorted to equidistribute the error. In 1989 Devloo [16] presented a 3-D adaptive finite element strategy for hexahedral elements. He demonstrated that a significant error reduction could be obtained by the adaptive grid refinement. Jeong and Yang [14, 17] proposed the adaptive grid refinement techniques for the 2-D analysis using the VOF method and for the 3-D analysis of the problems with simple geometric shape using the marker surface method.

In this study, the marker surface method and the adaptive grid refinement technique are employed in the 3-D finite element analysis of the filling stage in the die-casting process. Especially, the marker surface plugging technique and the marker surface regeneration technique incorporated in the marker surface method are proposed for the efficient analysis of 3-D practical problems. By a display technique in which the shaded images are sequentially combined into a final image, the molten metal flow field is effectively visualized. The marker surface method and the adaptive grid refinement technique are applied to a 3-D example for the benchmark test employed in the conference on the modeling of casting, welding and advanced solidification processes (MCWASP) VII [18]. The typical industrial problem of the die-casting process such as a cover of transmission case is analysed and the efficiency of the marker surface method and the adaptive grid refinement technique is discussed.

2. GOVERNING EQUATIONS

To analyse a 3-D transient melt flow, the continuity equation, the Navier–Stokes equation and the conduction equation are used as governing equations in the rectangular Cartesian co-ordinate system.
Continuity equation:

$$\frac{\partial u_i}{\partial x_i} = 0 \quad \text{in } \Omega \tag{1}$$

Navier–Stokes equation:

$$\rho \frac{\partial u_i}{\partial t} + \rho u_j \frac{\partial u_i}{\partial x_j} = \frac{\partial}{\partial x_j} \sigma_{ji}(u) + \rho f_i \quad \text{in } \Omega \tag{2}$$

where $\sigma_{ij} = -p\delta_{ij} + 2\mu d_{ij}, d_{ij} = \frac{1}{2}(\partial u_i/\partial x_j + \partial u_j/\partial x_i)$, $i = 1, 2$, and 3, and $j = 1, 2$, and 3. In the above equations, t, u_i, p, ρ, μ and f_i are the time, the velocity component in x_i direction, the pressure, the density, the dynamic viscosity and the body force, respectively. σ_{ij} and d_{ij} denote the stress and the strain rate tensors, respectively.
Heat conduction equation:

$$\rho c_p \left(\frac{\partial T}{\partial t} + u_i \frac{\partial T}{\partial x_i} \right) = \frac{\partial}{\partial x_i} \left(k_{ij} \frac{\partial T}{\partial x_j} \right) + Q \quad \text{in } \Omega \tag{3}$$

where T, c_p, k, and Q are the temperature, the specific heat, the thermal conductivity, and the heat source, respectively. On the free surface boundary $\partial\Omega_{\mathrm{s}}$, the Neumann boundary condition

$$\sigma_{\mathrm{n}} = -p + 2\mu_{\mathrm{air}} \frac{\partial u_{\mathrm{n}}}{\partial x_{\mathrm{n}}}, \quad \tau = \mu_{\mathrm{air}} \left(\frac{\partial u_{\mathrm{n}}}{\partial x_{\mathrm{t}}} + \frac{\partial u_{\mathrm{t}}}{\partial x_{\mathrm{n}}} \right) \quad \text{on } \partial\Omega_{\mathrm{s}} \tag{4}$$

is imposed where σ_{n}, τ, μ_{air}, subscripts n and t denote the normal stress, the shear stress, the dynamic viscosity of air, and the normal and tangential directions of the free surface boundary, respectively. On the free surface boundary, the surface tension, the viscous stress and the gas pressure are assumed to be zero in this study. Then the following slip condition is applied to the wall boundary $\partial\Omega_{\mathrm{wall}}$:

$$u_{\mathrm{n^w}} = 0 \quad \text{on } \partial\Omega_{\mathrm{wall}} \tag{5a}$$

where $u_{\mathrm{n}^{\mathrm{w}}}$ is the normal velocity component at the wall boundary. Then the following essential boundary condition is applied to the inflow boundary $\partial\Omega_{\mathrm{inf\ low}}$:

$$u_j = \bar{u}_j \quad \text{on } \partial\Omega_{\mathrm{inf\ low}} \tag{5b}$$

where $\bar{u}_j$ is the velocity component which is given at the inflow boundary. The initial conditions are given by specifying the velocity values at the initial time:

$$u_j = u_j^o \quad \text{on } \Omega \text{ at } t = 0 \tag{5c}$$

where u_j^o is the initial velocity component. On the surface boundaries $\partial\Omega_1$, $\partial\Omega_2$, and $\partial\Omega_3$, the temperature boundary conditions are given as

$$T = T_0 \quad \text{on } \partial\Omega_1, \quad k_{ij}\frac{\partial T}{\partial x_j} n_i = q \quad \text{on } \partial\Omega_2 \tag{6}$$

$$k_{ij}\frac{\partial T}{\partial x_j} n_i = -h(T - T_{\mathrm{neigh}}) \quad \text{on } \partial\Omega_3$$

where $\partial\Omega_1$, $\partial\Omega_2$, and $\partial\Omega_3$, are the temperature prescribed boundary, the heat flux prescribed boundary, and the convective boundary, respectively. T_0, q, h, and T_{neigh} are the prescribed temperature, the prescribed heat flux, the effective heat transfer coefficient and the temperature at the neighbor node on the interface boundary, respectively.

2.1. Finite element formulation

2.1.1. Transient flow field. Using the penalty-function formulation [19] in which the form

$$p = -\lambda \frac{\partial u_k}{\partial x_k} \tag{7}$$

is assumed for a large positive λ ($\sim 10^7\mu$), the finite element form of Equation (2) becomes

$$M_{i\alpha j\beta}\left(\frac{U_{j\beta}^{n+1} - U_{j\beta}^{n}}{\Delta t}\right) + C_{i\alpha j\beta}U_{j\beta} + N_{i\alpha}(u_i) = F_{i\alpha} + F_{i\alpha}^{\partial\Omega_{\mathrm{s}}} \tag{8}$$

where

$$M_{i\alpha j\beta} = \int_\Omega \rho\tilde{N}_\alpha N_\beta \delta_{ij}\,\mathrm{d}\Omega, \quad C_{i\alpha j\beta} = \int_\Omega (\lambda\tilde{N}_{\alpha,i}N_{\beta,j} + \mu\tilde{N}_{\alpha,j}N_{\beta,i} + \mu\delta_{ij}\tilde{N}_{\alpha,k}N_{\beta,k})\,\mathrm{d}\Omega$$

$$N_{i\alpha}(u_i) = \int_\Omega \rho\tilde{N}_\alpha u_k u_{i,k}\,\mathrm{d}\Omega, \quad F_{i\alpha} = \int_\Omega \tilde{N}_\alpha f_i\,\mathrm{d}\Omega, \quad F_{i\alpha}^{\partial\Omega_{\mathrm{s}}} = \int_{\partial\Omega_{\mathrm{s}}} N_\alpha\sigma_{\mathrm{n}}\,\mathrm{d}\Omega + \int_{\partial\Omega_{\mathrm{s}}} N_\alpha\tau\,\mathrm{d}\Omega$$

In the above equation, u_k is the velocity component, $U_{k\gamma}$ denotes the nodal value of u_k at the γth node, and N_γ means the shape function. Using the streamline-upwind/Petrov–Galerkin (SU/PG) formulation [20] the discontinuous shape function $\tilde{N}_\alpha$ can be defined as

$$\tilde{N}_\alpha = N_\alpha + \tilde{k}\bar{u}_j N_{\alpha,j}/|u| \tag{9}$$

where

$$\tilde{k} = (\tilde{\xi} u_\xi h_\xi + \tilde{\eta} u_\eta h_\eta + \tilde{\varsigma} u_\varsigma h_\varsigma)/2$$

$$\tilde{\xi} = \coth\ \alpha_\xi - 1/\alpha_\xi, \quad \tilde{\eta} = \coth\ \alpha_\eta - 1/\alpha_\eta, \quad \tilde{\varsigma} = \coth\ \alpha_\varsigma - 1/\alpha_\varsigma$$

$$\alpha_\xi = (e_\xi \cdot u) h_\xi / 2\mu, \quad \alpha_\eta = (e_\eta \cdot u) h_\eta / 2\mu, \quad \alpha_\varsigma = (e_\varsigma \cdot u) h_\varsigma / 2\mu$$

in which $\bar{u}_j = u_j/|u|$, e_ξ, e_η, and e_ς are the unit vectors, and h_ξ, h_η, and h_ς mean the element characteristic lengths in the local co-ordinate system of the master element for an eight-node hexahedral element. To solve Equation (8), the predictor–corrector method is used. The algorithm of the predictor–corrector method is summarized as follows:

Predictor

$$\tilde{u}_{n+1} = u_n + (1-\gamma)\Delta t a_n$$

$$u_{n+1}^{(0)} = \tilde{u}_{n+1} \tag{10}$$

Corrector
From $l = 0$ to $l = L$

$$\{(M_{i\alpha j\beta} + \gamma \Delta t C_{i\alpha j\beta}) U_{j\beta_{(n+1)}}^{(l+1)} = M_{i\alpha j\beta} \tilde{U}_{j\beta_{(n+1)}} + \gamma \Delta t (F_{i\alpha} - N_{i\alpha}(u_{i_{(n+1)}}^{(l)}))\} \tag{11}$$

$$a_{n+1} = \frac{(u_{n+1}^{L+1} - \tilde{u}_{n+1})}{\gamma \Delta t} \tag{12}$$

$$u_{n+1} = u_{n+1}^{(L+1)}$$

where u_n and a_n are the velocity and acceleration at the nth time iteration, respectively, Δt means the time increment, γ means a positive parameter which governs the stability and accuracy, l denotes the iteration number, and the total number of inner iterations is equal to $L+1$. A skyline solver [21] is employed for solving Equation (11).

2.1.2. Transient temperature field. Using the θ-method [22, 23] for time discretization, the heat conduction equation can be discretized as

$$M_{\alpha\beta}^T \frac{T_\beta^{n+1} - T_\beta^n}{\Delta t} + K_{\alpha\beta}^T (\theta T_\beta^{n+1} + (1-\theta) T_\beta^n) = F_\alpha^T \tag{13}$$

where

$$M_{\alpha\beta}^T = \int_\Omega \rho c_p N_\alpha N_\beta \, \mathrm{d}\Omega$$

$$K_{\alpha\beta}^T = \int_\Omega \rho c_p N_\alpha u_i N_{\beta,i} \, \mathrm{d}\Omega + \int_\Omega k_{ij} N_{\alpha,i} N_{\beta,j} \, \mathrm{d}\Omega + \int_{d\Omega_3} h N_\alpha N_\beta \, \mathrm{d}\Omega$$

$$F_\alpha^T = \int_\Omega N_\alpha Q \,\mathrm{d}\Omega + \int_{d\Omega_2} N_\alpha q \,\mathrm{d}\Omega + \int_{d\Omega_3} h N_\alpha T_{\mathrm{neigh}} \,\mathrm{d}\Omega$$

in which T_β is the nodal value of temperature at the βth node, θ is a parameter such that $0 \leqslant \theta \leqslant 1$, and the mass term M^T is lumped. The SU/PG formulation [21] for the heat conduction equation is used as the case of the Navier–Stokes equation.

In order to consider the effect of latent heat release, the following boundary condition is imposed on the interface region Γ of solid and liquid:

$$k_\mathrm{s} \frac{\partial T_\mathrm{s}}{\partial n} + k_\mathrm{l} \frac{\partial T_\mathrm{l}}{\partial n} = \rho L \frac{\partial X}{\partial t} \quad \text{on } \Gamma \tag{14}$$

where the subscripts s and l represent the solid and liquid phases, respectively, L means the latent heat and X is the position of the phase front. To treat the latent heat release, the temperature recovery method proposed by Tszeng *et al.* [24] is employed. In the temperature recovery method, the phase front is not continuously calculated and the heat release is not imposed as a moving boundary condition. The intermediate temperature is computed from the heat conduction equation without considering the latent heat boundary condition, and then the intermediate temperature is corrected into a solution.

3. MARKER SURFACE METHOD

In order to represent free surfaces accurately, to decrease memory storage and computation time, and to display predicted 3-D free surfaces, the marker surface method has been developed [17]. Whereas marker particles are distributed over a 3-D fluid region in the marker particle method, the marker surfaces representing predicted free surfaces directly are used in the method. The method has been successfully applied to the 3-D problems with simple geometric shape [17].

In this study, for the efficient analysis of the 3-D practical problems of complicated shape, the marker surface plugging technique and the marker surface regeneration technique are proposed. The procedure of the marker surface method can be introduced as follows, in which the proposed techniques and an adaptive grid refinement technique are incorporated.

Step I: The initial data are input and an initial marker surface is created. In the marker surface, the side length of a marker element should be short enough to represent an initial free surface.

Step II: The adaptive grid at the current time step is newly created by the grid refinement procedure and the grid coarsening procedure according to the refinement criteria such as an element category and a simple error estimator [25] in the internal region. The procedure is explained in Section 3.3.

Step III: In the adaptive grid, all elements are sorted into five types as follows:

- *Type* I: The internal element that is completely filled with fluid.
- *Type* II: The internal surface element that is completely filled with fluid and is adjacent to surface element.
- *Type* III: The surface element that is partially filled with fluid and contains any part of the marker surface.

Type IV: The external surface element that is empty with fluid, is adjacent to a surface element and contains no part of the marker surface.

Type V: The external element that is empty with fluid and contain no part of the marker surface.

Step IV: The grid of the fluid region is created which is composed of the internal elements, internal surface elements and surface elements.

Step V: By the FEM analysis the velocity field is obtained and marker nodes are advanced as follows:

$$x_m^{n+1} = x_m^n + u_m^{n+1}\Delta t \tag{15}$$

where x_m^{n+1} and x_m^n are the co-ordinates of the *m*th marker node at time steps $n+1$ and n, respectively, and u_m^{n+1} is the velocity of the *m*th marker node at time step $n+1$. The time increment Δt should be small enough to prevent the marker surface from escaping from the surface region composed of the internal surface, surface and external surface elements.

Step VI: The element types are changed due to the advancement of the marker surface.

(I) The internal surface element, surface element and external surface element are categorized into a newly defined set of unknown elements.
(II) The elements that comprise any part of the marker surface among the unknown elements become a surface element.
(III) If an unknown element is adjacent to an external element and an internal element, then the element is changed into a new external element and a new internal element, respectively. This procedure is repeated until no unknown element remains.
(IV) If an internal element and an external element are adjacent to surface elements then those are changed into an internal surface element and an external surface element, respectively.

Step VII: The marker surface plugging procedure is carried out in case of necessity. The procedure is explained in detail in Section 3.1.

Step VIII: Through the marker surface refinement procedure, the marker element with the sides of longer length than a given critical value is divided into two or four subelements [17].

Step IX: The procedure for the marker surface regeneration is accomplished in case of necessity. This procedure is explained in detail in Section 3.2.

Step X: The filling time step is increased. These procedures are iterated until the current filling time reaches the total time.

3.1. Marker surface plugging

In the analysis of a practical problem, in case the front of molten metal moves along a curved wall, the gap between the edge of a marker surface and the wall could be incrementally increased due to using bi-linear hexahedral elements. When any part of a marker element in a marker surface moves over a wall boundary, the marker element is erased from the marker surface. The erasing treatment makes a gap between the edge of marker surface and the wall boundary or between the split parts of marker surface, and the gap could also be increased by an expansion flow field.

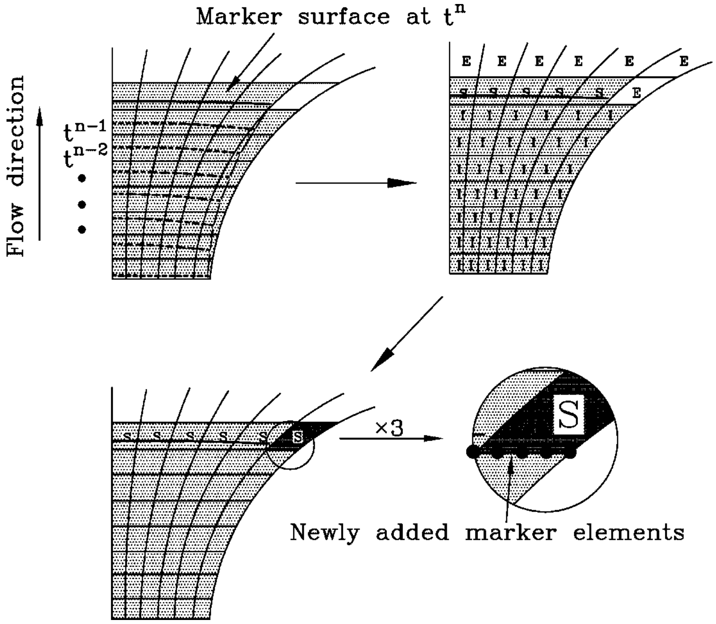

Figure 1. Marker surface plugging procedure.

When the gap becomes larger than the edge size of neighbouring elements and some parts of internal region come into contact with some parts of empty region without existing any surface region, the new parts of the marker surface are created on the intersectional area between both regions (Figure 1). The surface region includes any parts of the marker surface and distinguishes between the internal and empty regions. Through the marker surface plugging procedure, a marker element is newly created on a face edge shared by an internal element and an empty element. Then, the new marker element is refined until all sides of its subelements become shorter than the length prescribed for the marker surface refinement. The newly created parts of the marker surface are not connected with the existing part of the marker surface for efficient analysis, because a complicated technique and additional computation time are needed for their complete connection. Thus, several parts of marker surface can exist in the flow domain for the problems with complex shape.

3.2. Marker surface regeneration

In the marker surface method, the number of marker elements could exceed the limit number prescribed for efficient analysis because the number of marker elements is increased due to the marker surface refinement procedure and a great number of marker elements could be distributed in the surface and internal region. In this case, the marker surface is newly regenerated on the basis of its original shape in order to decrease the number of marker elements and computation time. The procedure for the marker surface regeneration can be introduced as follows (Figure 2):

Step I: In considering a surface element A being in contact with empty elements, a representative node representing all marker nodes belonging to the element A is created. The

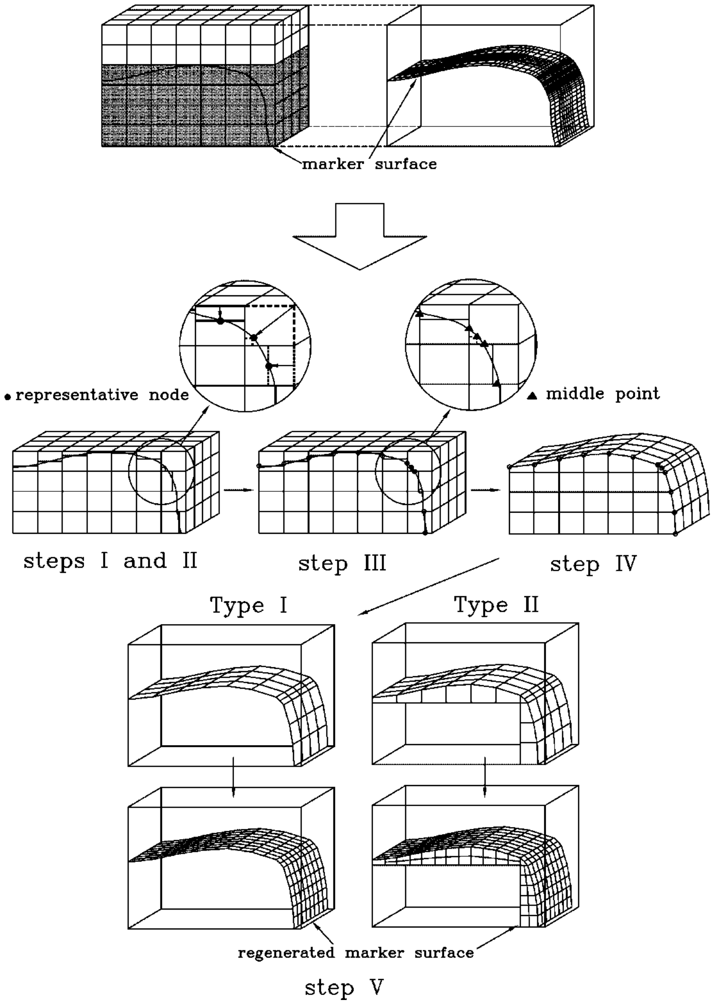

Figure 2. Marker surface regeneration procedure.

position of the representative node is computed from averaging the coordinate values of all marker nodes.

Step II: In the element A, the face side S_A in contact with the empty element is selected. If the opposite face side of S_A is in contact with the completely filled element, then the four nodes belonging to S_A are moved to the opposite face side along the edge sides until the moved S_A is in contact with the representative node. For all face sides in contact with the empty elements in the element A, this procedure is accomplished.

Step III: For all surface elements the steps I and II are accomplished. A node can have several newly created coordinates because it is independently moved in each of its neighbor elements. The final coordinate of the node is given by averaging the coordinates.

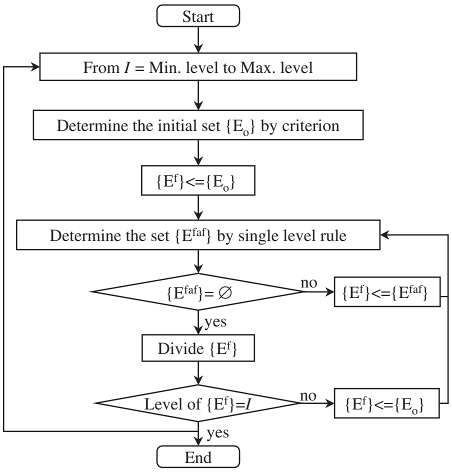

Figure 3. Flow chart of the refinement procedure.

Step IV: Each of all moved face sides becomes a new marker element. A regenerated marker surface is composed of the newly created marker elements.

Step V: According to the critical side length, the regenerated marker surface is refined.

3.3. Adaptive grid refinement

In the refinement criteria, there are an element category and the limit of the numerical error predicted by the simple error indicator [25]. As shown in Figure 3, if the category of an element, of which the refinement level is equal to the current level of the refinement loop, is the internal surface element, surface element or external surface element, or its predicted numerical error exceeds the prescribed value, then the element belongs to $\{E_0\}$. Each element belonging to $\{E_\mathrm{f}\}$ determined by the single level rule [15, 17] is divided into eight subelements. The coarsening criteria are the element category and the limit of the numerical error as was the case for the grid refinement. The coarsening procedure is accomplished incrementally from the maximum level to the minimum level as shown in Figure 4. If an element, of which the refinement level equals the current level of the coarsening loop, is an internal element or external element and its predicted numerical error does not exceed the prescribed value then it belongs to the temporary set $\{E^{\mathrm{temp}}\}$, which is used for the next sorting procedure. The eight elements belonging to each $\{E^{\mathrm{sf}}\}$ determined by the single level rule and the merging condition are merged into an element [17].

3.3.1. Error estimation in the internal fluid region. To estimate the numerical error of each element in the internal fluid region, the simple error estimator proposed by Zienkiewicz and Zhu [25] is employed. The L_2 norm of the numerical error is estimated by the following equation.

$$\|e\|_{L_2} = \left(\int_\Omega e^T e \,\mathrm{d}\Omega\right)^{1/2} = \left(\int_\Omega (\gamma_G - \gamma_h)^{\mathrm{T}}(\gamma_G - \gamma_h)\,\mathrm{d}\Omega\right)^{1/2} \tag{16}$$

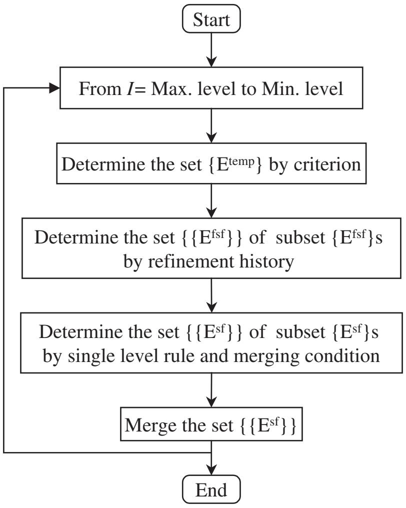

Figure 4. Flow chart of the coarsening procedure.

where γ is the strain tensor, γ_h and γ_G are the finite element solution and the least squares projection of γ_h, respectively. γ_G is discretized as

$$\gamma_G = \bar{\gamma}_{G_k} N_k \quad \text{in } \Omega$$

where $\bar{\gamma}_{G_k}$ is the nodal value of γ_{G_k} and N_k is the shape function. The finite element equation for $\bar{\gamma}_{G_k}$ is as follows:

$$\int_{\Omega} N_\alpha N_\beta \, \mathrm{d}\Omega \bar{\gamma}_{G_\beta} = \int_{\Omega} N_\alpha \gamma_h \, \mathrm{d}\Omega \tag{17}$$

$\|e\|_{L_2}/|u|_{\max}$ of each element is used as its predicted numerical error for the refinement procedure and coarsening procedure of internal fluid region.

4. NUMERICAL ANALYSIS RESULTS OF PROBLEMS

4.1. Benchmark test problem

A benchmark problem is analysed which was used for a voluntary test in the 7th conference on the MCWASP VII 1995 in Birmingham university [18]. The geometry of the problem consists of a simple plate with 15 mm thick and a narrow and tall filling system. The experiment of the problem was achieved by using a real time X-ray radiographics unit to visualize the flow of liquid aluminium in the sand mold cavity [18].

The material properties of pure Al and sand used for the analysis are shown in Table I. In order to analyse the problem efficiently, a pouring basin region is not contained in the region for the analysis and a stagnation pressure boundary condition is imposed at a sprue entrance, which is the intersectional area between the pouring basin and the sprue. The static head for calculation of the stagnation pressure value is taken to be 40 mm that is equal to the average

Table I. Thermophysical properties of pure Al and sand.

Properties	Molten metal (Al)	Mold (sand)
Density (g/cm^3)	2.385	1.52
Viscosity (poise)	1.3×10^{-2}	—
Conductivity (cal/cm/s/°C)	2.2×10^{-1}	1.5×10^{-3}
Specific heat (cal/g/°C)	2.56×10^{-1}	2.04×10^{-1}
Latent heat (cal/g)	95.0	—
Liquidus temperature (°C)	660.0	—
Solidus temperature (°C)	659.0	—

height of molten metal in the pouring basin during the experiment. The stagnation pressure can be obtained by

$$p_{\mathrm{s}} = \rho g h \tag{18}$$

where h is the static head. The initial temperatures of molten Al and sand, the room temperature, the gravity and the time increment used are 700, 25, 25°C, 9.8 m/s^2 and 0.8×10^{-3} s, respectively. The heat transfer coefficient between molten Al and sand is taken to be 1×10^{-3} cal/cm^2/s/°C and the heat transfer coefficient between sand and air is given by 1×10^{-4} cal/cm^2/s/°C. The surface refinement level is taken to be 1. On the wall boundary, the slip boundary condition including tangential wall stress is imposed, and the model for the tangential wall stress proposed by Dhatt *et al.* [26] is employed. In the model, the tangential wall stress is calculated as follows:

$$f_t = \rho \frac{|u_t| u_t}{C^2} \tag{19}$$

where $C = A \ln y^+ E = A \ln y^+ + B$, $A = 2.5, y^+ \geqslant 90$. In the above equation, y^+ is the slip velocity vector, the coefficient C depends on the rugosity and node position, and E is the rugosity coefficient. The constants B and y^+ are given by 5.5 and 100, respectively. In this problem the value of Weber number, ratio of inertia forces to surface tension forces,

$$We = \frac{\rho\, \mathrm{d} U^2}{\sigma} \tag{20}$$

is larger than 60, where d is the half width of the gate ($= 3$ cm), U is the characteristic velocity ($= 100$ cm/s), and σ is the surface tension coefficient ($= 1.2$ N/m) [18]. Thus, the effect of surface tension is neglected. The turbulent effect is also not considered because it is difficult to find reasonable parameter values for turbulent models such as the mixing-length model and the $k - \varepsilon$ model. The element configurations of the initial grids of the cavity and the mold are shown in Figure 5. The numbers of nodes and elements of casting part in the initial grid are 1486 and 826, respectively. The grid of the mold part consists of 12 611 nodes and 10 052 elements. The critical number of marker elements for the marker surface regeneration is taken to be 8000. As shown in Figure 5, the mold is composed of the backside and frontside parts. In the mold, a symmetric plane does not exist because only the backward part of the mold contains the cavity. Thus, the total region of the casting and mold has to be analysed. A fixed grid is used for Case I, while an adaptive grid is used for

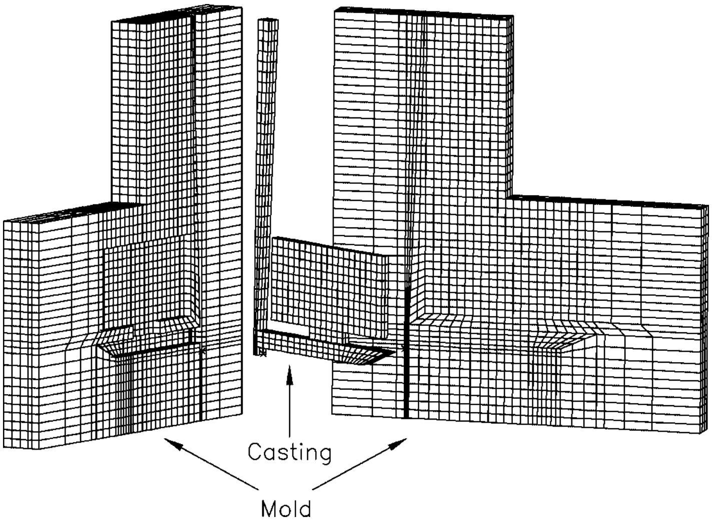

Figure 5. Element configurations of the initial grids for the casting and the mold.

Case II. Plate 1 shows the approximated fluid regions at the prescribed time steps for Cases I and II, respectively. The predicted 3-D fluid region with free surface at each time step is effectively displayed by a new display technique, in which the shaded images of the total cavity region, approximated fluid region and marker surface are independently created by a shading treatment and those are sequentially combined into a final image. Generally, in the previous studies, for the 3-D display of fluid and empty regions in the cavity region, the total cavity region has been represented by wire frame. These numerical results are compared with the experimental results [18] in Figure 6. The predicted filling trending is similar to that of the experiment. At the filling step I, the backward filling in the runner is predicted in both cases. However, the phenomenon of air bubble formation in the interface between the gate and runner is more distinctly predicted in Case II. The air bubbles are formed in the region in which the overlying reflected stream and underlying stream are joined together in the runner. The jumping phenomenon at the filling step II is shown only in Case II and the shapes of fluid regions at intermediate filling steps in Case II are closer to the experimental results than those in Case I. Figure 7 shows the element configurations of the fluid grids generated from the fixed grid and adaptive grid. It is shown that the finer elements are efficiently distributed over the surface region defined by the element category criterion, the specific region defined by the error criterion in the internal region and the gate region that is a specific region defined for obtaining the stable numerical results. The initial error tolerance and $u_{\max}$ used for the simple error estimator are 2.3×10^{-2} and 3 m/s, respectively. As shown in Table II the element density of the surface region and specific regions increases by eight times through the adaptive grid refinement while the average number of elements of the total domain grid increases by 3.2 times and computation time increases by 5.4 times. From these results the efficiency of the adaptive grid refinement technique is sufficiently proven.

In Figure 8 the temperature distributions obtained immediately after the filling stage in the front surface, middle plane and back surface of the casting are shown. It is shown that

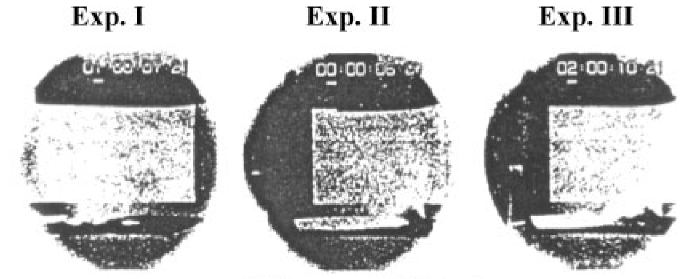

Filling step I (0.50 sec)

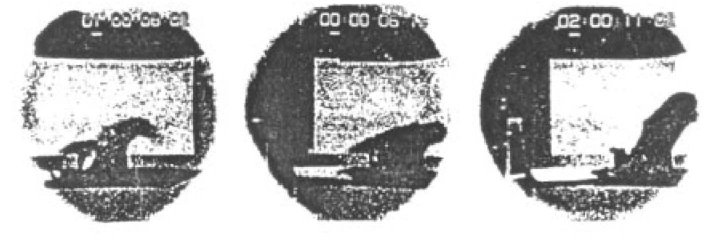

Filling step II (0.74 sec)

Filling step III (1.00 sec)

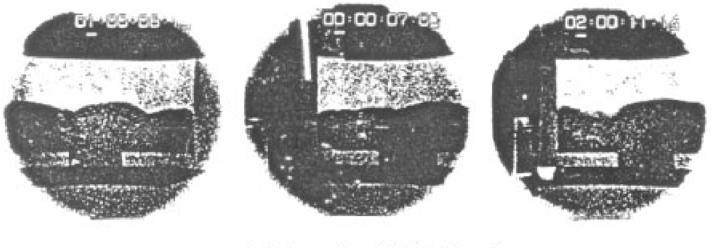

Filling step IV (1.24 sec)

Figure 6. Frames from X-ray video showing the filling of the runner and mold cavity [18].

the pattern of temperature distribution is very similar to the flow pattern because the pattern is highly dependent on the velocity field during the filling stage. This result shows that the temperature field in the filling stage is also improved by using the adaptive grid because the flow pattern is predicted more exactly by using the adaptive grid, as compared with the fixed grid.

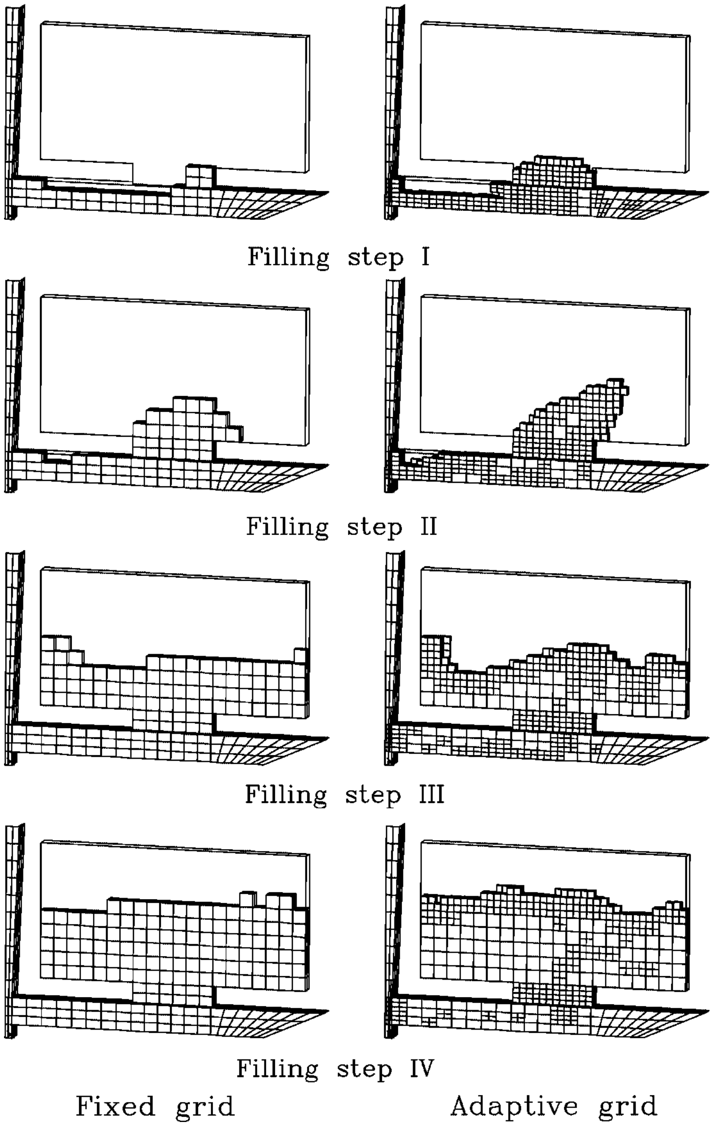

Figure 7. Element configurations at the given filling steps.

4.2. *Practical application to the die-casting process*

A cover of transmission case as a typical industrial problem of the die-casting process is analysed. In Figure 9, the shapes of cavity part and gate system and the injection direction at biscuit gate are shown. The thickness of lower and upper bottoms of die cavity is 2.3 mm, the dimensions of the biscuit gate are 40 × 10 mm, and the overall dimensions of the cavity part are 219.9 × 175.7 × 51.1 mm. The ADC12 to be an Al alloy is used as a molten metal material and the material properties of the ADC12 are shown in Table III. The temperature

Table II. Comparison of the results between two cases for the benchmark test problem.

		Fixed grid	Adaptive grid
Relative element density of the surface region and the specific internal region		1	8
Average number of elements	Grid of fluid domain	496 (1)	1,572 (3.2)
	Grid of total domain	826 (1)	2,524 (3.1)
Relative computation time		1	5.4

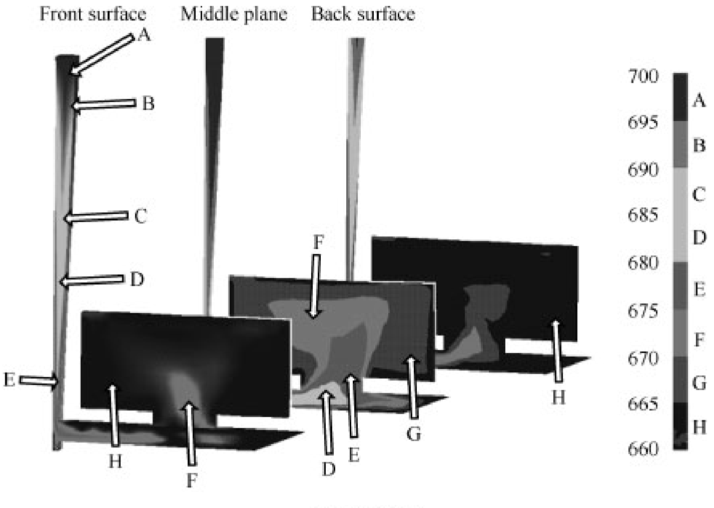

Fixed grid

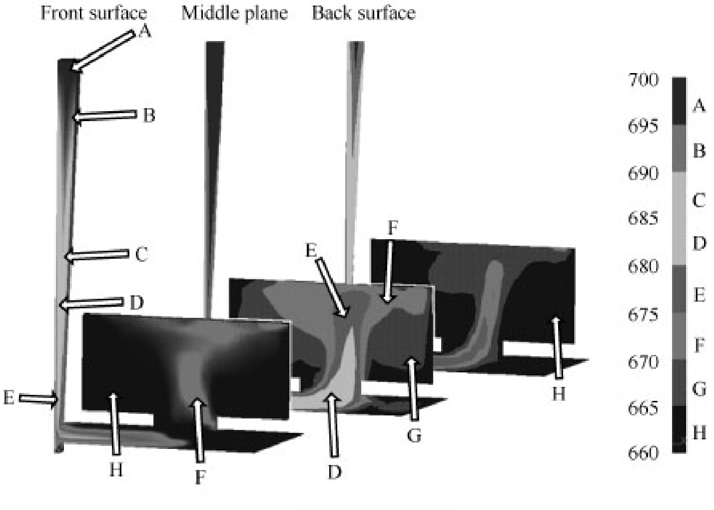

Adaptive grid

Figure 8. Predicted temperature distributions in the casting at the end of the filling stage.

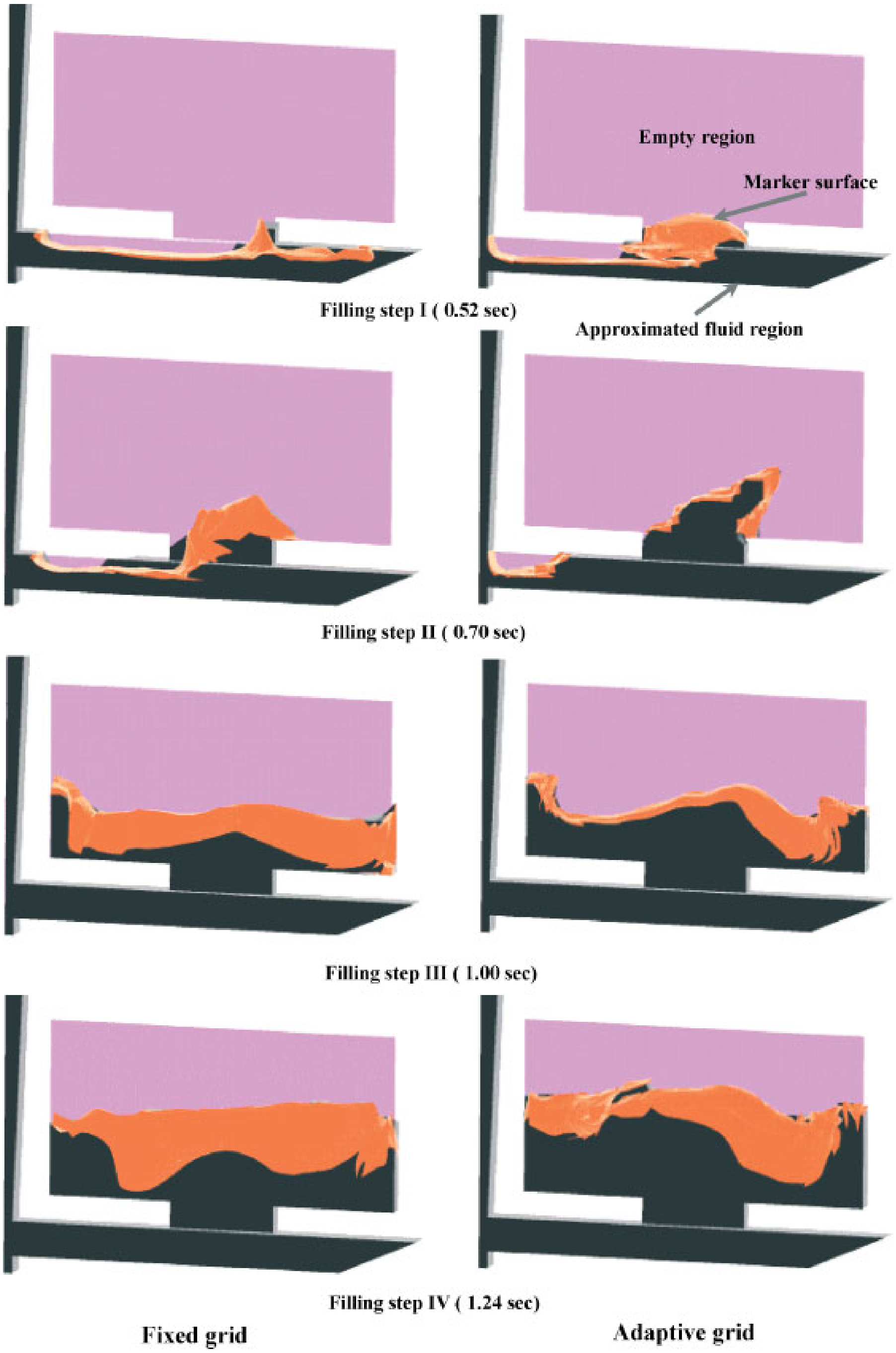

Plate 1. Simulated mold filling sequence.

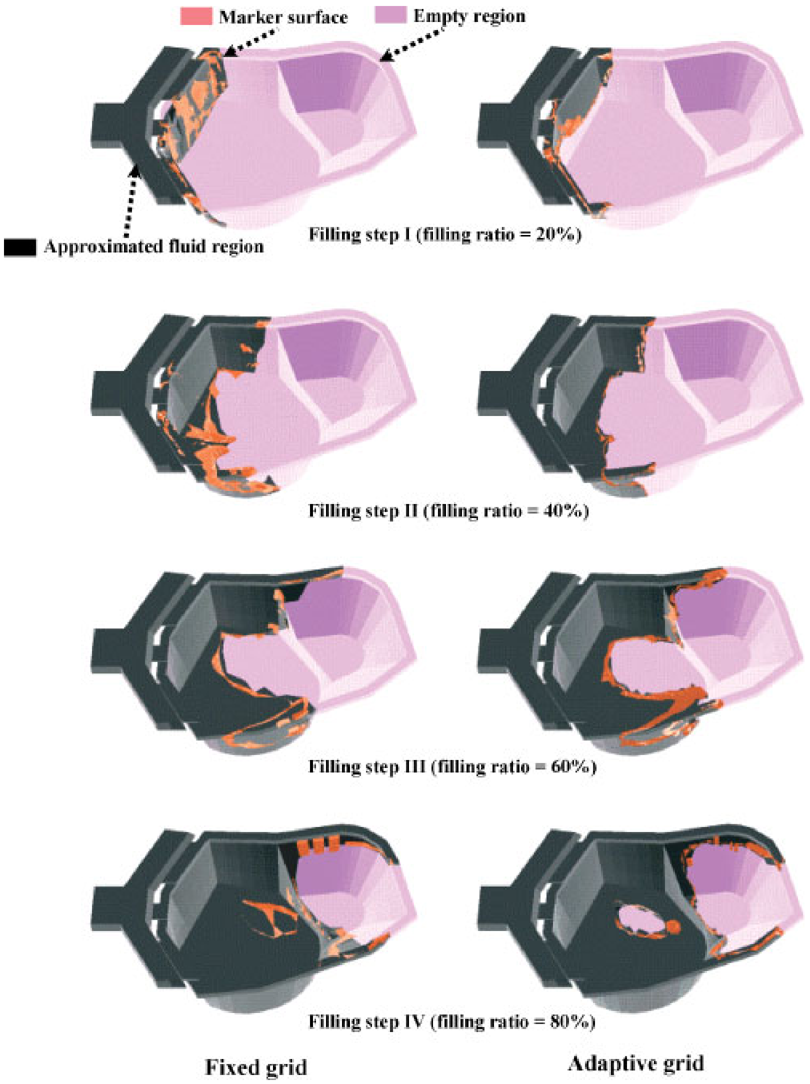

Plate 2. Simulated mold filling sequence.

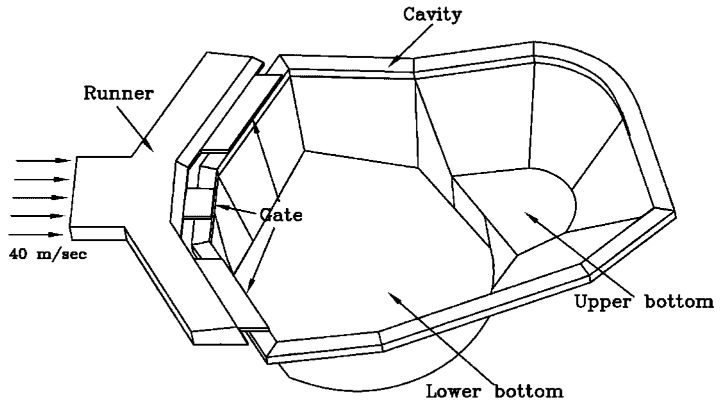

Figure 9. Boundary condition and the geometries of the die cavity and the runner system.

Table III. Thermophysical properties of Al alloy (ADC12).

Properties	Molten metal (Al alloy—ADC12)
Density (g/cm^3)	2.8
Viscosity (poise)	1.3×10^{-2}
Conductivity (cal/cm/s/°C)	2.3×10^{-1}
Specific heat (cal/g/°C)	2.4×10^{-1}
Latent heat (cal/g)	94
Liquidus temperature (°C)	580
Solidus temperature (°C)	520

of the die with cavity is assumed to be constant because the cooling system is installed inside the die and the cycle time of the die-casting process is very short. The initial temperatures of the die and molten metal are 250 and 650°C, respectively. The time increment for the filling analysis is taken to be 0.8×10^{-6} s. The heat transfer coefficient between die surface and molten metal and the gravity acceleration are $0.2\,\text{cal/cm}^2/\text{s}/°\text{C}$ and $9.8\,\text{m/s}^2$, respectively. In order to consider the tangential wall stress the constants B and y^+ for the model proposed by Dhatt *et al.* [26] are given by 5.5 and 100, respectively. The effect of surface tension is not considered in this problem because the value of Weber number calculated from Equation (20) is 1.9×10^6 where d is the half width $(= 0.02\,\text{m})$ of the gate at the central position among three gates, U is the characteristic velocity $(= 2.0 \times 10^2)$, and σ is the surface tension coefficient $(= 1.2\,\text{N/m})$.

The fixed grid is used for Case I, while the adaptive grid is used for Case II. In this analysis, the limit value for the marker surface regeneration is taken to be 10 000. Plate 2 shows the results for Cases I and II. The overall flow patterns in both cases show good consistency. However, as compared to the flow patterns in Case I, the flow patterns in Case II using the adaptive grid are more dynamic and reasonable because the refined elements are effectively distributed in the surface and internal regions. At the filling step IV, the flow pattern in Case II enables one to visualize obviously the air entrapped region at the lower bottom while in Case I only some parts of the marker surface remain in the region.

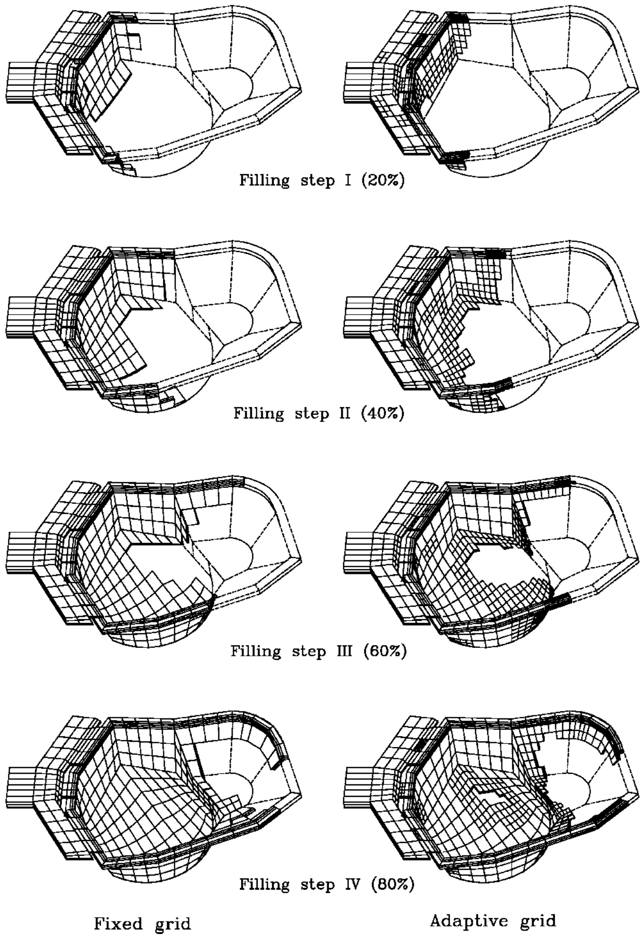

Figure 10. Element configurations at the given filling steps.

Table IV. Comparison of the results between two cases for the practical problem.

		Fixed grid	Adaptive grid
Relative element density of the surface region and the specific internal region		1	8
Average number of elements	Grid of fluid domain	652 (1)	1550 (2.4)
	Grid of total domain	1020 (1)	2280 (2.2)
Relative computation time		1	5.6

In the classical marker particle method, it is difficult to calculate the volume of the fluid region and to visualize the fluid region at each time step because the fractional volume of each element is not calculated. In the marker surface method, the approximate fluid region based on the position of the marker surface is created through performing Steps I–III in the

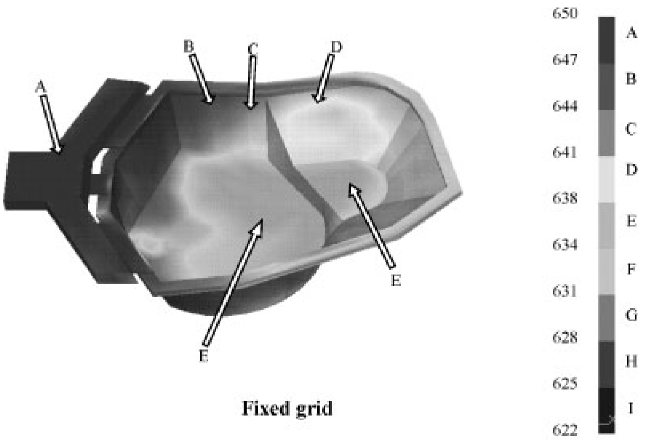

Fixed grid

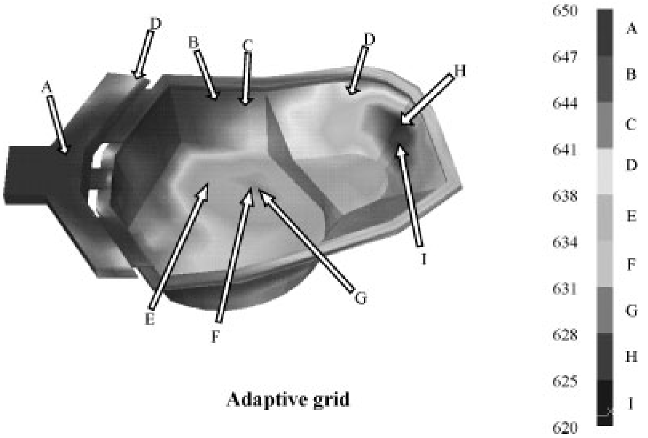

Adaptive grid

Figure 11. Predicted temperature distributions at the end of the filling stage.

marker surface regeneration technique. And the volume of fluid region can be approximately predicted by calculating the volume of the approximate fluid region. It is shown that the free surfaces of the approximate fluid regions in Case II are closer to the marker surfaces than those in Case I because the shape of the approximate fluid region is directly affected by the element size of the surface region. It can be shown that the marker surfaces are discontinuous while those are continuous in the numerical results of the previous example. The causes of this result may be summarized as follows. First, the marker surface moving along a curved wall could be broken apart, because some marker elements near the wall surface are erased from the marker surface in case those are moved outside the cavity region due to the use of the linear hexahedral elements in the initial grid. Secondly, after the marker surface plugging procedure is accomplished, the gap between an existing marker surface and newly generated marker elements exists.

Figure 10 shows the element configurations for the grids of fluid regions. It can be shown that refined elements are efficiently distributed over the surface region defined by the element category criterion and also over the specific region defined by the error criterion in the internal region. The initial error tolerance and $|u|_{\max}$ used are 3.0×10^{-2} and 1.5×10^{2}m/s, respectively. In this analysis, the value of the error tolerance is automatically changed during the filling stage, because the number of elements to be divided due to the error criterion is limited to the values ranging from 80 to 320. The prescription of the limit is required for increasing the stability of the analysis, since the velocity field may be suddenly changed at each time step. The gap between the maximum and minimum numbers prevents the error criterion from too frequent changes. As shown in Table IV the element density of the surface region and also of the specific region in the internal region increases by eight times through the adaptive grid refinement, while the average numbers of elements for the grid of the total domain increases by 2.2 times and the computation time increases by 5.6 times. From these results the effectiveness of the adaptive grid refinement in the analysis of this practical problem is satisfactorily verified.

In Figure 11, it is shown that the overall flow pattern can be predicted by the temperature distribution immediately after the filling stage because the temperature distribution is highly dependent on the flow pattern. Figure 11 shows that the air-entrapped region can be indirectly predicted because the temperature of molten metal is relatively low in the region where the molten metal is finally filled. The temperature of molten metal is also relatively low in the region in which the flow of molten metal is stagnated, cavity thickness is thin, or the edges of cavity are included. The minimum temperature obtained by using the adaptive grid is lower than that by using the fixed grid, because refined elements in the adaptive grid are distributed over the surface region and the specific internal region, and the temperature variation of each element is much sensitive to its edge length in thickness direction.

5. CONCLUSIONS

In this work, the marker surface plugging technique and marker surface regeneration technique have been proposed for efficient 3-D analysis and have been incorporated in the marker surface method. Through the marker surface plugging technique, new parts of marker surface are created on the intersectional area on which some parts of internal region come into contact with some parts of empty region. By using the marker surface regeneration technique, the marker surface for which the number of marker elements exceeds the prescribed limit is regenerated on the basis of its original shape in order to decrease the number of marker elements and computational time. By a new display technique in which the shaded images which correspond to the die cavity, the fluid region and the marker surface are sequentially combined into a final image, molten metal flow field has been visualized effectively. Through the marker surface method and the adaptive grid refinement technique a 3-D example used as the benchmark test of the conference on the MCWASP VII has been analysed. The numerical results have shown good agreement with the experimental results and the efficiency of the adaptive grid refinement has been verified. A typical industrial problem of the die-casting process such as a cover of transmission case has been analysed. It has been thus shown that the proposed techniques and the adaptive grid refinement technique can be effectively applied to general industrial problems. If the turbulent effect is considered for the analysis of the cover of transmission case, then more complicated phenomena may be predicted. Considering the turbulent effect could be important for obtaining reasonable results for 3-D industrial problems.

REFERENCES

1. Harlow FH, Welch JE. Numerical calculation of time-dependent viscous incompressible flow of fluid with free surface. *Physics of Fluids* 1965; **8**:2182–2189.
2. Amsden AA, Harlow EH. The SMAC method: a numerical technique for calculating incompressible fluid flows. *Los Alamos Scientific Laboratory Report* LA-4370, University of California, 1970.
3. Hwang WS, Stoehr RA. Molten metal flow pattern prediction for complete analysis of near net shape casting. *Materials Science and Technology* 1988; **4**:240–250.
4. Anzai K, Niyama E. Quasi three-dimensional mold filling simulation system for prediction of defects in die castings. In *Modeling of Casting*, *Welding and Advanced Solidification Processes*, vol. IV, Giamei AF, Abbaschian GJ (eds). The Minerals, Metals and Materials Society: Davos, Switzerland, 1988; 471–485.
5. Anzai K, Uchida T. Mold filling patterns of flat plate die castings. In *Modeling of Casting*, *Welding and Advanced Solidification Processes*, vol. V, Rappaz M, Özgü MR, Mahin KW (eds). The Minerals, Metals and Materials Society: Davos, Switzerland, 1990; 741–748.
6. Hwang JD, Lin HJ, Su KC. Mathematical modeling of fluid flow during vertical centrifugal casting. In *Modeling of Casting*, *Welding and Advanced Solidification Processes*, vol. V, Rappaz M, Özgü MR, Mahin KW (eds). The Minerals, Metals and Materials Society: Davos, Switzerland, 1990; 725–732.
7. Nomura H, Terashima K. Computer simulation of die casting filling process and model experiment. In *Proceedings of the First Pacific Rim International Conference on Modeling of Casting and Solidification Processes*, Hong CP, Niyama E, Hwang WS (eds). Yonsei University: Seoul, Korea, 1991; 153–162.
8. Chen CW, Chou HY, Li CR, Shei CT, Hwang WS. Comparison of different computational fluid dynamics techniques on their applications to the modeling of mold filling in casting. *Transactions of the Japan Foundrymen's Society* 1993; **12**:94–106.
9. Zaidi K, Abbes B, Teodosiu C. Finite element simulation of mold filling using marker particles and the k–ε model of turbulence. *Computer Methods in Applied Mechanics and Engineering* 1997; **144**:227–233.
10. Hwang WS, Stoehr RA. Molten metal flow pattern prediction for complete analysis of near net shape casting. *Materials Science and Technology* 1988; **4**:240–250.
11. Chen S, Johnson DB, Raad PE. The surface marker method. In *Computational Modeling of Free and Moving Boundary Problems*, *Fluid Flow*, vol. 1. De Gruyter: New York, 1991; 223–234.
12. Nichols BD, Hirt CW. Calculating three-dimensional free surface flows in the vicinity of submerged an exposed structures. *Journal of Computational Physics* 1973; **12**:234–246.
13. Wang SS, Stuhmiiler JH. Modified partial-cell method for free-surface incompressible flow simulation. *Numerical Heat Transfer* 1980; **3**:209–223.
14. Jeong JH, Yang DY. Finite element analysis of transient fluid flow with free surface using VOF (Volume of Fluid) method and adaptive grid. *International Journal for Numerical Methods in Fluids* 1998; **26**:1127–1154.
15. Oden JT, Strouboulis T, Devloo P. Adaptive finite element methods for the analysis of inviscid compressible flow: part I: fast refinement/unrefinement and moving mesh methods for unstructured meshes. *Computer Methods in Applied Mechanics and Engineering* 1986; **59**:327–362.
16. Devloo PR. A three dimensional adaptive finite element strategy. *Computers and Structures* 1989; **38**:121–130.
17. Jeong JH, Yang DY. Three dimensional finite element analysis of transient fluid flow with free surface using marker surface method and adaptive grid refinement. *International Journal for Numerical Methods in Fluids* 1998; **29**:657–684.
18. Sirrel B, Holliday M, Compbell J. The benchmark test for the 7th conference on the modeling of casting, welding and advanced solidification processes 1995. In *Modeling of Casting, Welding and Advanced Solidification Processes VII*, Cross M, Cambell J (eds). The Minerals, Metals and Materials Society: London, England, 1995; 915–1013.
19. Hughes TJR, Liu WK, Brooks A. Finite element analysis of incompressible viscous flows by the penalty function formulation. *Journal of Computational Physics* 1979; **30**:1–60.
20. Brooks AN. Streamline Upwind/Petrov-Galerkin formulations for convection dominated flows with particular emphasis on the incompressible Navier–Stokes equations. *Computer Methods in Applied Mechanics and Engineering* 1982; **32**:199–259.
21. Kikuchi N. *Finite Element Methods in Mechanics*. Cambridge University Press: New York, USA, 1986.
22. Wood WL, Lewis RW. A comparison of time marching schemes for the transient heat conduction equation. *International Journal for Numerical Methods in Engineering* 1975; **9**:679–689.
23. Dalhuijsen AJ, Segal A. Comparison of finite element techniques for solidification problems. *International Journal for Numerical Methods in Engineering* 1986; **23**:1807–1829.

24. Tszeng TC, Im YT. Kobayashi S. Thermal analysis of solidification by the temperature recovery method. *International Journal of Machine Tools and Manufacture* 1989; **29**:107–120.
25. Zienkiewicz OC, Zhu JZ. A simple error estimator and adaptive procedure for practical engineering analysis. *International Journal for Numerical Methods in Engineering* 1987; **24**:337–357.
26. Dhatt G, Gao DM, Cheikh AB. A finite element simulation of metal flow in moulds. *International Journal for Numerical Methods in Engineering* 1990; **30**:821–831.